SUPPLEMENTARY INFORMATION

Momentum-resolved electronic structure at a buried interface from soft x-ray standing-wave angle-resolved photoemission

A. X. Gray,[1,2,3] J. Minár,[4] L. Plucinski,[5] M. Huijben,[6] A. Bostwick,[7] E. Rotenberg,[7] S.-H. Yang,[8] J. Braun,[4] A. Winkelmann,[9] G. Conti,[1,2] D. Eiteneer,[1,2] A. Rattanachata,[1,2] A. A. Greer,[1,2] J. Ciston,[10] C. Ophus,[10] G. Rijnders,[6] D. H. A. Blank,[6] D. Doennig,[11] R. Pentcheva,[11] J. B. Kortright,[2] C. M. Schneider,[5] H. Ebert,[4] and C. S. Fadley[1,2]

[1]*Department of Physics, University of California Davis, Davis, California 95616, USA*

[2]*Materials Sciences Division, Lawrence Berkeley National Laboratory, Berkeley, California 94720, USA*

[3]*Stanford Institute for Materials and Energy Science, Stanford University and SLAC National Accelerator Laboratory, 2575 Sand Hill Road, Menlo Park, California 94029, USA*

[4]*Department of Chemistry, Physical Chemistry Institute, Ludwig Maximillian University, Münich, Germany*

[5]*Peter-Grünberg-Institut PGI-6, Forschungszentrum Jülich GmbH, 52425 Jülich, Germany*

[6]*Faculty of Science and Technology, MESA$^+$ Institute for Nanotechnology, University of Twente, Enschede, The Netherlands*

[7]*Advanced Light Source, Lawrence Berkeley National Laboratory, Berkeley, California 94720, USA*

[8]*IBM Almaden Research Center, San Jose, California 95120, USA*

[9]*Max-Planck-Institut für Mikrostrukturphysik, Weinberg 2, D-06120 Halle (Saale), Germany*

[10] *National Center for Electron Microscopy, Lawrence Berkeley National Laboratory, Berkeley, California 94720, USA*

[11] *Department of Earth and Environmental Sciences and Center of Nanoscience (CENS), Ludwig Maximillian University, Münich, Germany*

We here present some supplementary materials related to our method of sample growth, measurement technique, data analysis, the several levels of theoretical modeling we have done, and the more detailed properties or our sample. This includes our method of correcting for x-ray photoelectron diffraction modulations in the ARPES results, as well as some additional theoretical results to clarify the basic electronic structures of LSMO and STO and what we expect to see in experiment, some fully self-consistent LDA+U results for the multilayer, and further clarifications concerning the one-step

photoemission calculations that are our major interpretive tool. These provide additional insights into the validity and interpretation of our experimental data. In addition, we present supplementary characterization measurements of our LSMO/STO superlattice sample, which include magnetization, electrical transport, and high-resolution cross-sectional STEM analysis with imaging by both high-angle annular dark field (HAADF) and electron energy loss spectroscopy (EELS).

Superlattice growth and characterization

The LSMO/STO superlattice sample consisted of 120 bilayers, nominally consisting of 4 unit cells of LSMO (~15.51 Å) and 4 unit cells of STO (~15.61 Å), and was fabricated using the PLD technique, with reflection high-energy electron diffraction (RHEED) for monitoring the growth process. Atomically smooth TiO_2-terminated STO(100) substrates were prepared by a combined HF-etching/anneal treatment [1]. All substrates had vicinal angles of ~0.1°. A stoichiometric LSMO target and a single-crystal STO target were ablated at a laser fluence of 1.5 J/cm^2 and a repetition rate of 1 Hz. During growth, the substrate was held at 750 °C in an oxygen environment at 2.6×10^{-1} mbar. The growth process was optimized in a previous study so as to result in an ideal unit-cell-controlled layer-by-layer growth and bulk-like magnetic and transport properties [2]. A low level of surface roughness (maximum of 4 Å) was confirmed by atomic force microscopy (AFM). Out-of-plane superlattice periodicity was confirmed to be 31.13 Å using x-ray diffraction (XRD), very close to the expected bilayer thickness of 31.12 Å. An analysis of rocking curves in a prior SW-XPS study of a similar multilayer confirmed the high quality, although noting a decrease in the bilayer period as growth continued [3], an effect confirmed below by TEM. Clear ferromagnetic behavior was observed up to room temperature in a SQUID Magnetometer.

Angle-resolved photoemission measurements

The photoelectrons were analyzed by means of a hemispherical analyzer (VG Scienta R4000) equipped with a two-dimensional microchannel plate (MCP) detector [4]. A six-axis sample manipulator permitted rotations in both the take-off angle θ_{TOA} and the orthogonal angle β_{TOA}. Small corrections to the

incidence angle θ_{inc} due to the rotation in β_{TOA} were also made. The Fermi level was frequently calibrated using a Au reference sample. In presenting detector images, ~2.5° of the detector angle range (corresponding to ~0.75 Å^{-1} in k_x) on both sides of each (k_x, k_y) map was cropped in order to remove experimental artifacts associated with the detector edges.

It might be noted that the angular positions of the Bragg features for the rocking curves in fig. 1(c) of the main text deviate somewhat (by ~1°) from those reported in our previous study of a similar, but thinner, multilayer sample (48 LSMO/STO bilayers, compared to the 120 bilayers of the sample in the current study) [ref. 17 in the paper]. This deviation is due to a combination of the variation in the bilayer thickness with successive layers, as discussed in a prior study [3] and below in connection with our TEM results, and an improved procedure for calibrating the incidence x-ray angle. The angles here are thus more accurate.

Correction of data for x-ray photoelectron diffraction and density-of-state effects, and bulk-interface difference maps

In fig. S2(a) we show a typical (k_x, k_y) photoemission intensity distribution obtained in the LSMO-bulk-sensitive geometry ($\theta_{inc} = 12.4°$) for a fixed binding energy of about -2.5 eV, which corresponds to the binding energy of Mn 3d t$_{2g}$–derived states [5,6]. At this binding energy, we need not consider any contribution of the STO overlayer to spectra, since STO has the bandgap of ~3.25 eV, and therefore does not have states in this energy range [ref. 6, also see theoretical calculations in figs. S6-S8 below]. We do, however, have to consider that, to whatever degree this spectrum involves a mixture of $\vec{k}$ -conserving direct transitions (DTs) and phonon-induced non-direct transitions (NDTs), the NDT components will have energy distributions reflecting the DOS and angular distributions corresponding to core-like x-ray photoelectron diffraction (XPD), as discussed elsewhere [7,8]. As noted in the main text of our paper, correction for DOS and XPD effects can to first order be done by dividing the data successively by the average over angle and the average over energy of each detector image, respectively [9] as demonstrated for experimental data from W and GaAs recently [10,11]. At 20 K, the fraction of DTs is estimated from

3

the ARPES Debye-Waller factor to be ~75%, and thus NDTs, or in turn, XPD- and DOS-like effects, to be ~25% of the total intensity. In order to further separate the effects of true electronic-state dispersions from XPD, we have also measured the angle-resolved spectra of the Mn $3p$ core-level concurrently with the valence-band measurements for each incidence angle. Core levels represent localized states with no dispersion in $\vec{k}$. Thus, the Mn $3p$ pattern we see in fig. S2(b) is exclusively due to XPD, and this is confirmed by a dynamical Kikuchi-band XPD calculation shown in fig. S2(c) [12], which exhibits excellent agreement with the data of fig. S2(b). By now correcting the SWARPES spectrum in fig. S2(a) using the XPD-only spectrum in fig. S2(b), through a scaled division described in more detail in the next paragraph, we can finally unambiguously isolate the $\vec{k}$-resolved electronic structure of Mn $3d$ t_{2g}-derived states. But we stress that our conclusions regarding interface-specific electronic state dispersions do not depend critically on this correction procedure, as discussed further in connection with difference data in figs. S3-S5 below.

In correcting our SWARPES raw data for the effects of x-ray photoelectron diffraction and density-of-states effect induced by phonon-induced non-direct transitions, each detector image in (k_x, k_y) was first divided by the average over angle and average over energy, as described in the main text [9,10,11]. Then, to remove any remaining XPD contributions, which are estimated to be about 25% of intensity based on the Debye-Waller factor calculation, we performed a scaled normalization of the combined Mn $3d$ t_{2g} + XPD (k_x, k_y) maps using angle-resolved spectra of the Mn $3p$ core-level at a binding energy of 42.2 eV and a kinetic energy very close to the valence photoelectrons (~791 eV compared to ~833 eV):

(1) Averages of the valence-band $\vec{k}$-space maps for more localized flat-band and XPD-like bands 3 and 4 at the binding energies of 4.0 eV and 6.2 eV were taken, and several brightest and darkest diffraction spots on these averaged VB maps were selected (4 brightest and 3 darkest). (2) Mn $3p$ XPD maps were scaled such that the same diffraction spots on these maps match the intensities of the selected diffraction spots on the averaged valence-band maps for each experimental geometry. (3) These scaled Mn $3p$ maps

were then used to normalize the valence-band maps for each corresponding experimental geometry by simple subtraction, thus assuming a linear addition of bandlike dispersive effects and XPD effects. Such a normalization procedure also removes any signature of the 2D detector non-uniformity, a purely instrumental effect.

Additional aspects of the analysis of our data make it clear that this correction was reliable and did not introduce any artifacts in the final LSMO bulk-minus-interface SWARPES difference results. In fig. S1, we first show the complete set of angles at which SWARPES data was obtained, indicated on top of the core-level rocking curves that were used to determine the most bulk LSMO and most LSMO/STO interface sensitive angles, denoted as C and E on the figure. From the standing wave plot in fig. S1(c), we can thus say that angles A, B, C should be more interface sensitive and angles E, F, G more bulk sensitive, with D being somewhere in between.

In figs. S3-S5, we show the bulk-interface differences of SWARPES data for different pairs of angles, so as to either emphasize the difference, or minimize it by looking at two bulk or two interface angles. All of the data has here been corrected for XPD effects using the procedure described above. Fig. S3 represents two angles expected to be sensitive to bulk LSMO, and these differences show essentially no discernible fine structure. Fig. S4 is for the two angles showing maximum standing-wave contrast between bulk and interface, as shown already in fig. 2(d) of the main text; clear differences are seen for the e_g, t_{2g}, and valence-band bottom panels that we finally assign to LSMO, which are expected to show the biggest effects. Fig. S5 represents two angles expected to be sensitive to the LSMO/STO interface, and here again, there is no discernible fine structure. We thus conclude that we are able to reliably measure the ca. 5% effects that are differences between the bulk and the interface electronic structure.

Reference band structure calculations and first-order simulations:

Band structure calculations for the band insulator STO and the half-metallic ferromagnet LSMO, as calculated with the Wien2k program in the LDA (for STO) and LDA+U (for LSMO) approximation [13], are shown in fig. S6, (a) and (b). For LSMO, we have used an effective U equal to the Mn 3d onsite

Coulomb parameter U minus the Mn exchange parameter J of 2.0 eV. In fig. S6(c), the orbital-projected densities of states for LSMO are also shown. The STO conduction-band states have been shifted using the so-called scissor operator so as to yield the experimental 3.3 eV indirect band gap. The two band structures have also been shifted relative to one another by the experimental valence-band offset of 3.0 eV, as measured using a standard x-ray photoemission (XPS) technique based on valence-band and core-level spectra excited by hard x-rays from our multilayer and from the two bulk materials STO and LSMO of which it is made [14,15]. This band offset is also in good agreement with a 2.73 eV value calculated within LDA+U for the actual 4 unit cell/4 unit cell multilayer structure, using the all-electron method described in the next section. This plot makes it clear that we can expect to see Mn e_g and t_{2g} derived states over ca. 0-3 eV binding energy. At this level of bulk theory, it is not clear whether the valence band minimum of STO or LSMO will be lower in energy, but we clarify this below.

The expected contributions of LSMO and STO versus binding energy in our spectra have also been estimated through these bulk densities of states by assuming that each LSMO or STO layer of thickness *t* in the multilayer contributes an intensity proportional to *[1-exp(-t/$\Lambda_e$sinθ_{TOA})]*, where Λ_e is the inelastic mean free path in that layer (as estimated from the TPP-2M formula [16]), and that this intensity is reduced by all overlying layers of thickness t' according to *exp(-t'/$\Lambda_e$sinθ_{TOA})*. Each orbital-projected layer DOS has also been multiplied by atomic differential photoelectric cross sections to approximately allow for matrix-element effects. The results of these calculations are shown in fig. S7, where they are compared to angle-integrated experimental spectra that should approximate matrix-element weighted densities of states; these are shown for the two angles that maximize sensitivity to the LSMO/STO interface and bulk LSMO. These calculations further confirm that we expect to see LSMO bands over ca. 0-3 eV, and that STO will dominate at ~75% or more for larger binding energies. The relative intensities of peaks 1 and 2 in the experimental data also nicely confirm the enhancement of the LSMO-derived features when the standing-wave moves to the central LSMO bulk-sensitive position, further verifying our overall methodology.

Fully self-consistent electronic structure calculations for the multilayer:

For a more accurate look at the electronic structure of our sample, we have also carried out fully self-consistent density functional theory calculations on LSMO/STO superlattices of our ideal 4 unit cell/4 unit cell configuration (see fig. S8(a) using the all electron full-potential augmented plane-wave method in the WIEN2k implementation [13]. Electronic correlations beyond the generalized gradient approximation (GGA) [17] were considered in the LDA/GGA+U method [18] with U = 3.0 eV, J = 0.7 eV on Mn 3*d* states, U = 5.0 eV, J = 1.0 eV on Ti 3*d* states and U = 8.0 eV, J = 0.0 eV on La 4*f* states. The statistical distribution of La and Sr was treated in the virtual crystal approximation. The rhombohedral LSMO bulk structure was also transformed to monoclinic to fit on the $SrTiO_3$(001) substrate and the lateral lattice parameter of the superlattice was set to the GGA-lattice constant of $SrTiO_3$ (3.92×√2 Å). Full relaxation of the internal structural parameters was performed in an 80-atom unit cell, allowing for all octahedral tilts and rotations.

Some of these results are shown in fig. S8, including in (b) the spin-resolved layer-by-layer total density of states, with Mn-containing layers representing the two interfaces (IF) and the two internal (IF-1) or bulk LSMO layers indicated. The energy locations 1-5 of the points at which we have chosen to present SWARPES results are also indicated. These calculations indicate that the changes in DOS from the interface to internal/bulk regions of LSMO are subtle, but certainly present. From the atomic identities in the idealized layer structure shown, it is also clear that the top and bottom interfaces are not identical, and the consequences of this are also evident in the TEM results we show below. The projected Mn densities of states shown in fig. S8(c) also indicate marked differences between the multilayer and bulk LSMO, as well as between interface and internal/bulk LSMO layers in the multilayer. These results also indicate that the intensity from the SWARPES results at energy 5, the bottom of the valence bands, should arise predominantly from LSMO, as we have modeled it in our free-electron final-state calculations (cf. fig. 4(a) in the main text). The difference in this aspect from the theoretical results in fig. S6 is no doubt due to the more complete set of U and J parameters used here, thus better allowing for correlation effects. The bandgap of STO is also better predicted in fig. S8 for the same reason.

Optimization of atomic positions also indicates in results not shown here that there is a Jahn-Teller effect in the interface octahedra that is fully consistent with a prior core-level SW-XPS study [3], and that the octahedra are compressed along z, rather than elongated, and show a strong orbital polarization of ~8.4%, with stronger occupation of d_{x2y2}; this polarization is also found to be much smaller (~1.7%) and of opposite sign in the internal/bulk layers. Future SWARPES measurements with variable light polarization should permit directly measuring such effects.

One-step theory of photoemission calculations:

Self-consistent electronic structure calculations were first performed within the ab-initio framework of spin-density functional theory. The electronic structure was calculated in a fully relativistic mode by solving the corresponding Dirac equation. This was achieved using the spin polarized relativistic multiple-scattering or Korringa-Kohn-Rostoker formalism [19]. To account for electronic correlations beyond the LSDA [20] we employed a LSDA+U scheme as implemented within the relativistic SPR-KKR formalism, including for LSMO the average screened Coulomb interaction U (an adjustable parameter, chosen as $U_{Mn} = 2.0$ eV) and the Hund exchange interaction J (calculated directly and set to $J_{Mn} = 0.9$ eV) [21] and for STO $J_{Ti} = 0.9$ eV. Substitutional disorder has been treated within the coherent potential approximation, which is considered to be the best available single-site alloy theory. The effective potentials were treated within the atomic sphere approximation (ASA). A sample consisting of repeated 4 unit cells of LSMO/4 unit cells of STO was used to calculate self-consistently the electronic structure of the corresponding semi-infinite half-space, thus yielding the effective potentials. Our photoemission calculations are based on these electronic structure inputs. Lifetime effects in the initial and final states have been included via imaginary values of the potential $V_{i,f}$. To take care of impurity scattering a small constant imaginary value of $V_{ii} = 0.08$ eV was used for the initial states. For the final states, a constant imaginary part $V_{if} = $ ~3.0 eV has been chosen to simulate the IMFP for our photon energy, corresponding to an inelastic mean free path for intensity of about 19 Å. Furthermore, the layer-resolved photocurrent was weighted layer-by-layer with the corresponding electric-field intensity $|E^2|$

profile of the standing wave inside the superlattice as a function of depth and incidence angle as derived from our optical model (cf. fig. 1(c) in the main text). Finally, the current was averaged over a 300 meV energy window, which corresponds to the experimental data binning.

We note here that the band structures and densities of states initially calculated in deriving the atomic potentials for the SPR-KKR method agree well with those in fig. S7. A further important point is that the full multilayer was included in these calculations, so that the effects of scattering of electrons originating in the LSMO layers by the STO interlayers and final STO overlayer were explicitly included. However, since phonon effects leading to non-direct transitions and DOS+XPD effects [7,8] were not included in the calculations, it is still appropriate to have corrected our experimental data for these effects. Also, no allowance was made for the relaxation of atomic positions near the interface, although this is an obvious point for future investigation and we have in the separate set of calculations described above begun to explore this.

Magnetization and Electrical Transport Measurements:

Electrical transport properties of the sample were measured using the four-point-probe technique, and are shown in fig. S9(a). The magnetic properties of the sample were measured in a Quantum Design SQUID Magnetometer (MPMS). Figs. S9(b),(c) show the temperature dependence of the saturation magnetization (b) and typical magnetization curves at 10 K and 290 K (c) along the [100] direction after magnetic field cooling at 1 Tesla from 360 K. The values of T_c, resistivity and saturation magnetization are all consistent with prior studies of LSMO/STO multilayers in this thickness range [22].

High-Resolution Cross-Section STEM Measurements:

In order to verify with a direct imaging technique our previous standing-wave rocking-curve analysis of concentration depth profiles in a similar STO/LSMO multilayer, as reported previously in ref. 17 of our letter [3], we have performed high-resolution cross-sectional STEM measurements with both high-angle annular dark field (HAADF) and electron energy loss spectroscopy (EELS), using the aberration-corrected TEAM 0.5 microscope at the National Center for Electron Microscopy. utilizing a

remote operation computer station (RemoTEAM) located at the Electron Microscopy Center at Argonne National Laboratory. The results of these measurements are shown in fig. S10 below. From the quantitative analysis of intensities of over 800,000 atomic columns across the full 120 bilayer cross-section, we have measured the interfacial roughness/interdiffusion between the LSMO and STO layers to be 1 - 1.5 u.c. This result is further confirmed by directly measuring the EELS chemical signal ratio of Ti/Mn in several smaller regions of the film, with the LSMO-on-STO interface exhibiting slightly more interdiffusion/roughness than the STO-on-LSMO interface. Furthermore, the layer thickness is directly measured to be 4.0 unit cells at the beginning of the growth process, but is found to decrease to 3.4 unit cells at the 120th bilayer. Thus, the STEM results fully confirm our prior SW-XPS finding that there is a gradient in the thickness of the STO and LSMO layers from top to bottom of the superlattice [3], and attest to the accuracy of the multilayer optical constants that we have used for our simulations.

References

1. Koster, K. *et al*. Quasi-ideal strontium titanate crystal surfaces through formation of strontium hydroxide. *Appl. Phys. Lett.* **73** (1998) 2920.

2. Huijben, M. *et al*. Critical thickness and orbital ordering in ultrathin $La_{0.7}Sr_{0.3}MnO_3$ films. *Phys. Rev. B* **78** (2008) 094413.

3. Gray, A. X. *et al*. Interface properties of magnetic tunnel junction $La_{0.7}Sr_{0.3}MnO_3/SrTiO_3$ superlattices studied by standing-wave excited photoemission spectroscopy. *Phys. Rev. B* **82** (2010) 205116.

4. Wannberg, B. Electron optics development for photo-electron spectrometers, *Nucl. Instrum. Methods Phys. Res., Sect. A* **601** (2009) 182.

5. Chikamatsu, A. *et al*. Band structure and Fermi surface of $La_{0.6}Sr_{0.4}MnO_3$ thin films studied by *in situ* angle-resolved photoemission spectroscopy. *Phys. Rev. B* **73** (2006) 195105.

6. Kumigashira, H. *et al*. *In situ* resonant photoemission characterization of $La_{0.6}Sr_{0.4}MnO_3$ layers buried in insulating perovskite oxides. *J. Appl. Phys.* **99** (2006) 08S903.

7. Plucinski, L. *et al*. Band mapping in higher-energy x-ray photoemission: Phonon effects and comparison to one-step theory. *Phys. Rev. B* **78** (2008) 035108.

8. Papp, C. *et al*. Band mapping in x-ray photoelectron spectroscopy: An experimental and theoretical study of W(110) with 1.25 keV excitation. *Phys. Rev. B* **84** (2011) 045433.

9. A. Bostwick and E. Rotenberg, private communication.

10. Gray, A. X. *et al*. Probing bulk electronic structure with hard X-ray angle-resolved photoemission, *Nature Mater.* **10** (2011) 759.

11. Gray, A. X. *et al*. Bulk electronic structure of the dilute magnetic semiconductor $Ga_{1-x}Mn_xAs$ through hard X-ray angle-resolved photoemission. *Nature Mater.* **11** (2012) 957.

12. Winkelmann, A., Fadley, C. S. and Garcia de Abajo, F. J. High-energy photoelectron diffraction: model calculations and future possibilities. *New. J. Phys.* **10** (2008) 113002.

13. Blaha, P., Schwarz, K., Madsen, G., Kvasnicka, D. & Luitz, J. *WIEN2k, An Augmented Plane Wave + Local Orbitals Program for Calculating Crystal Properties* (Karlheinz Schwarz, Techn. Universit. Wien, 2001) ISBN 3-9501031-1-2.

14. Chambers, S. A., Droubay, T., Kaspar, T. C. & Gutowski, M. Experimental determination of valence band maxima for $SrTiO_3$, TiO_2, and SrO and the associated valence band offsets with Si(001). *J. Vac. Sci. Tech. B* **22** (2004) 2205.

15. Conti, G. *et al*. Valence band offset in an LSMO/STO multilayer. *unpublished*.

16. Tanuma, S., Powell, C. J. & Penn, D. R. Calculations of electron inelastic mean free paths. IX. Data for 41 elemental solids over the 40 eV to 30 keV range. *Surf. Interface Anal.* **43** (2011) 689.

17. Perdew, J. P., Burke, K. & Ernzerhof, M. Generalized Gradient Approximation Made Simple. *Phys. Rev. Lett.* **77** (1996) 3865.

18. Anisimov, V. I., Solovyev, I. V., Korotin, M. A., Czyzyk, M. T. & Sawatzky, G. A. Density-functional theory and NiO photoemission spectra. *Phys. Rev. B* **48** (1993) 16929.

19. Ebert, H., Koedderitzsch, D. and Minár. Calculating condensed matter properties using the KKR-Green's function method — recent developments and applications. J. Rep. Prog. Phys. **74** (2011) 096501.

20. Jones, R. O. and Gunnarsson, O. The density functional formalism, its applications and prospects. Rev. Mod. Phys. **61** (1989) 689.

21. Minar, J. *et al*. Multiple-scattering formalism for correlated systems: A KKR-DMFT approach. Phys. Rev. B **72**, 045125 (2005); Minar, J. *et al*. Correlation effects in transition metals and their alloys studied using the fully self-consistent KKR-based LSDA + DMFT scheme. J. Phys.: Cond. Mat. **23** (2011) 253201.

22. Fitting Kourkoutis, L., Song, J. H., Hwang, H. Y., & Muller, D. A. Microscopic origins for stabilizing room-temperature ferromagnetism in ultrathin manganite layers. *P. Natl. Acad. Sci.* **107** (2010) 11682.
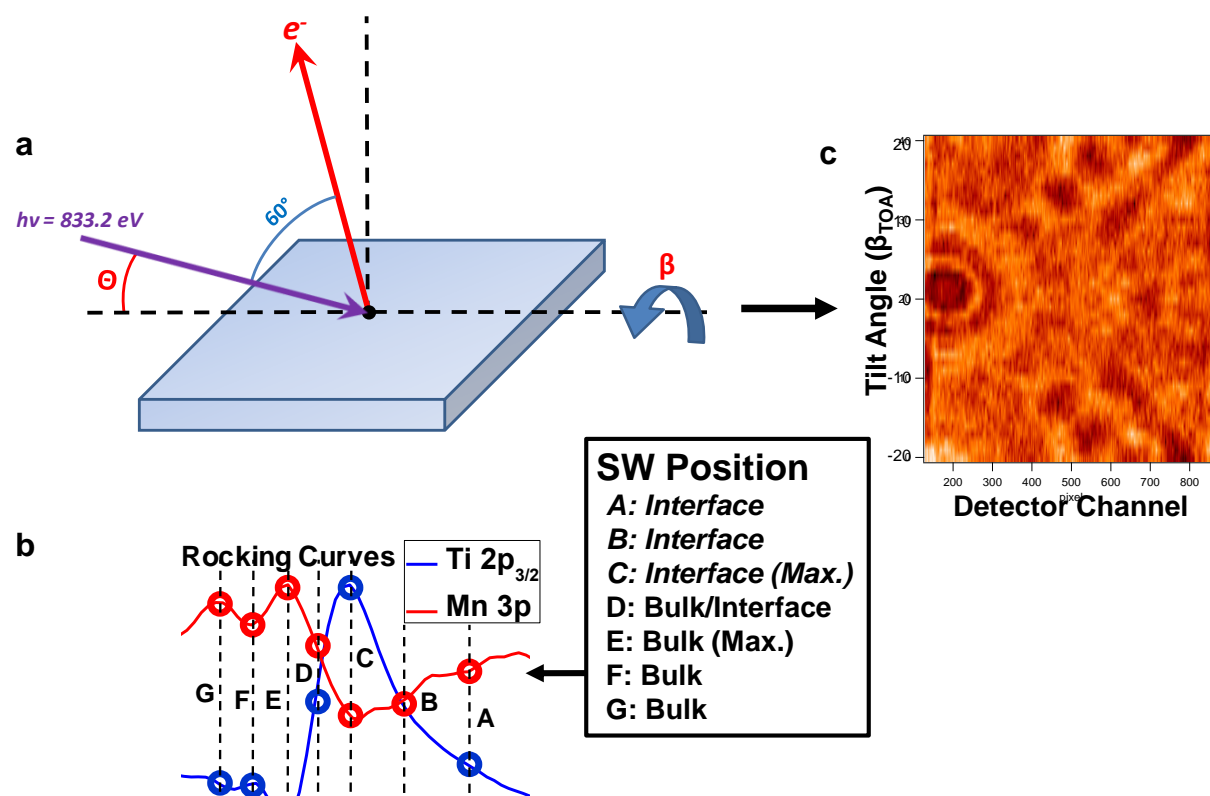
Figure S1

Fig. S1. (a) Our measurement geometry. (b) The seven different grazing incidence angles (Θ) at which SWARPES data were collected, corresponding to various positions along the Ti $2p_{3/2}$ and Mn $3p$ rocking curves. (c) For each value of Θ, an ARPES measurement was collected at 40 different tilt angles (β_{TOA}) ranging from -20° to +20°, finally yielding corrected data as shown here for the example energy at point 2 expected to be dominated by Mn t_{2g} states.

Figure S2
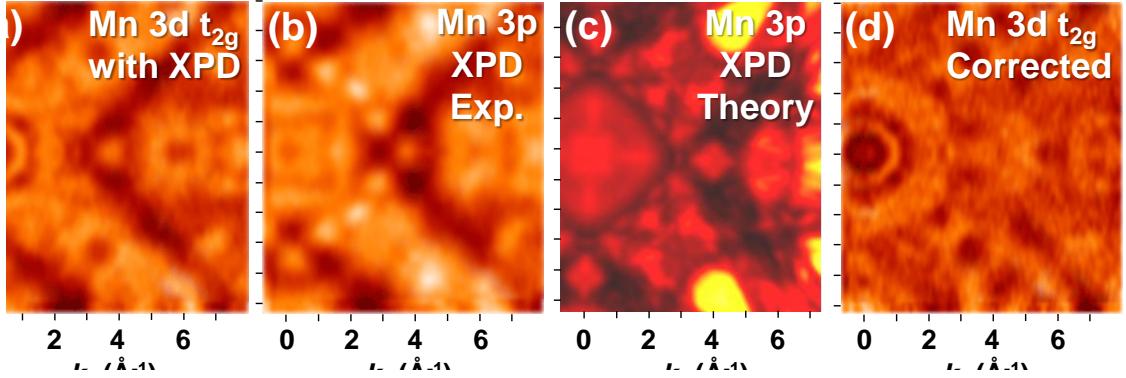
Fig. S2. Separating band-dispersions in SWARPES from residual x-ray photoelectron diffraction. (a) A typical (k_x, k_y) map for a fixed value of binding energy E_B , integrated over a 300 meV window containing the Mn $3d$ t_{2g} valence states, including an estimated 25% of intensity due to x-ray photoelectron diffraction (XPD). (b) A corresponding (k_x, k_y) XPD map of the Mn $3p$ core-level exhibiting only XPD modulation. (c) A simulation of the Mn $3p$ XPD pattern using dynamical diffraction (Kikuchi-band) theory. (d) The corrected (k_x, k_y) map obtained by normalizing the combined Mn $3d$ t_{2g} + XPD spectrum in (a) by the XPD spectrum in (b), so as to more clearly obtain the dispersive electronic structure of the Mn $3d$ t_{2g} states, via method described in detail above.

Figure S3
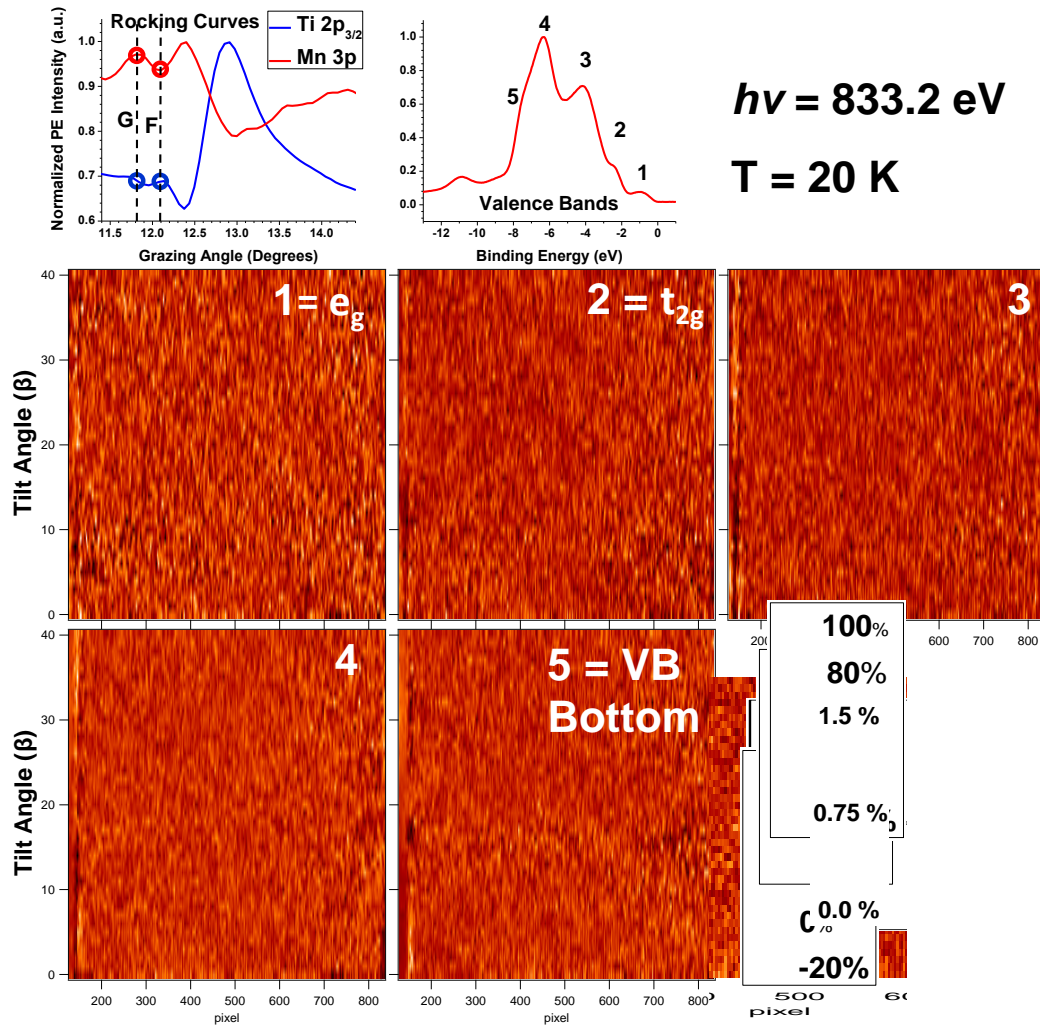
Fig. S3. Difference SWARPES patterns between angles F and G that should both be more sensitive to bulk or central LSMO, with the angular positions relative to the Ti $2p_{3/2}$ and Mn $3p$ rocking curves and energy positions in a density-of-states shown in the top two panels. The relative magnitude of the intensity modulations is also indicated.
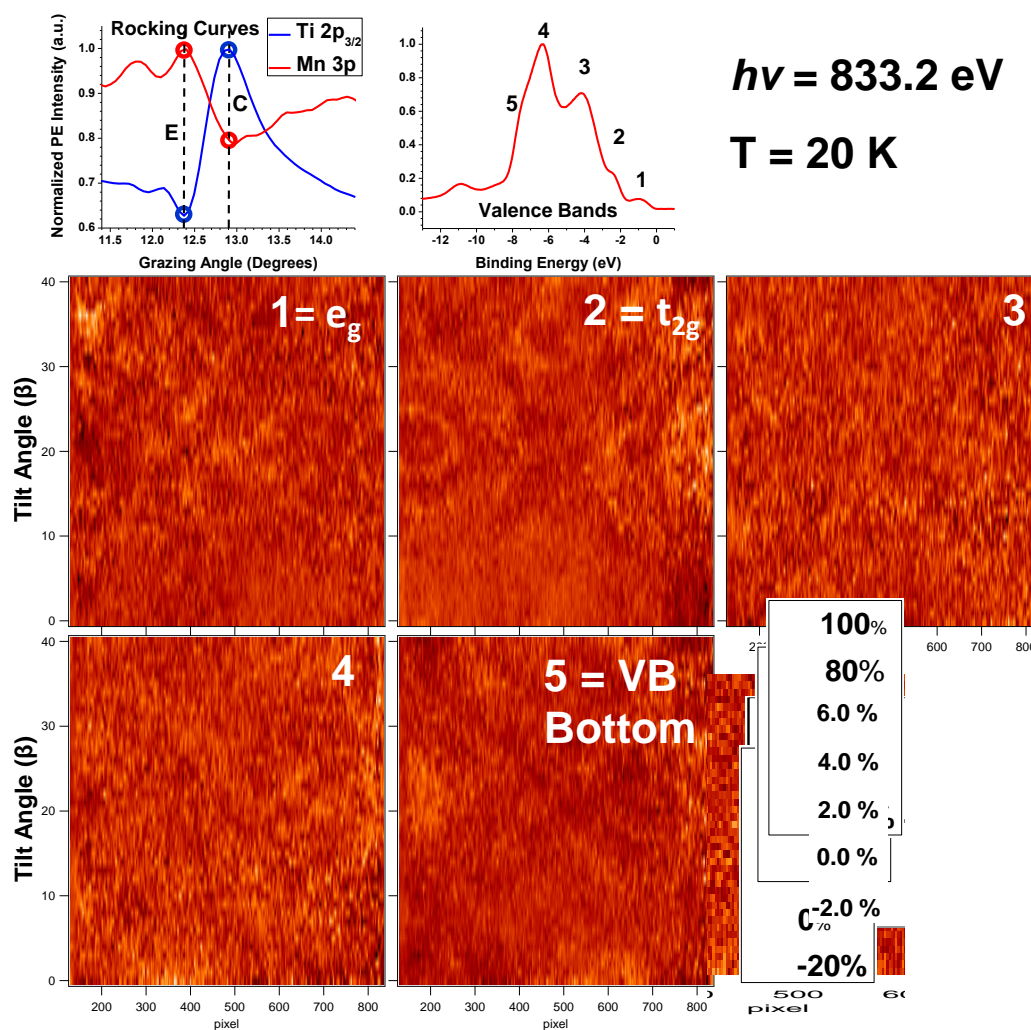
Figure S4

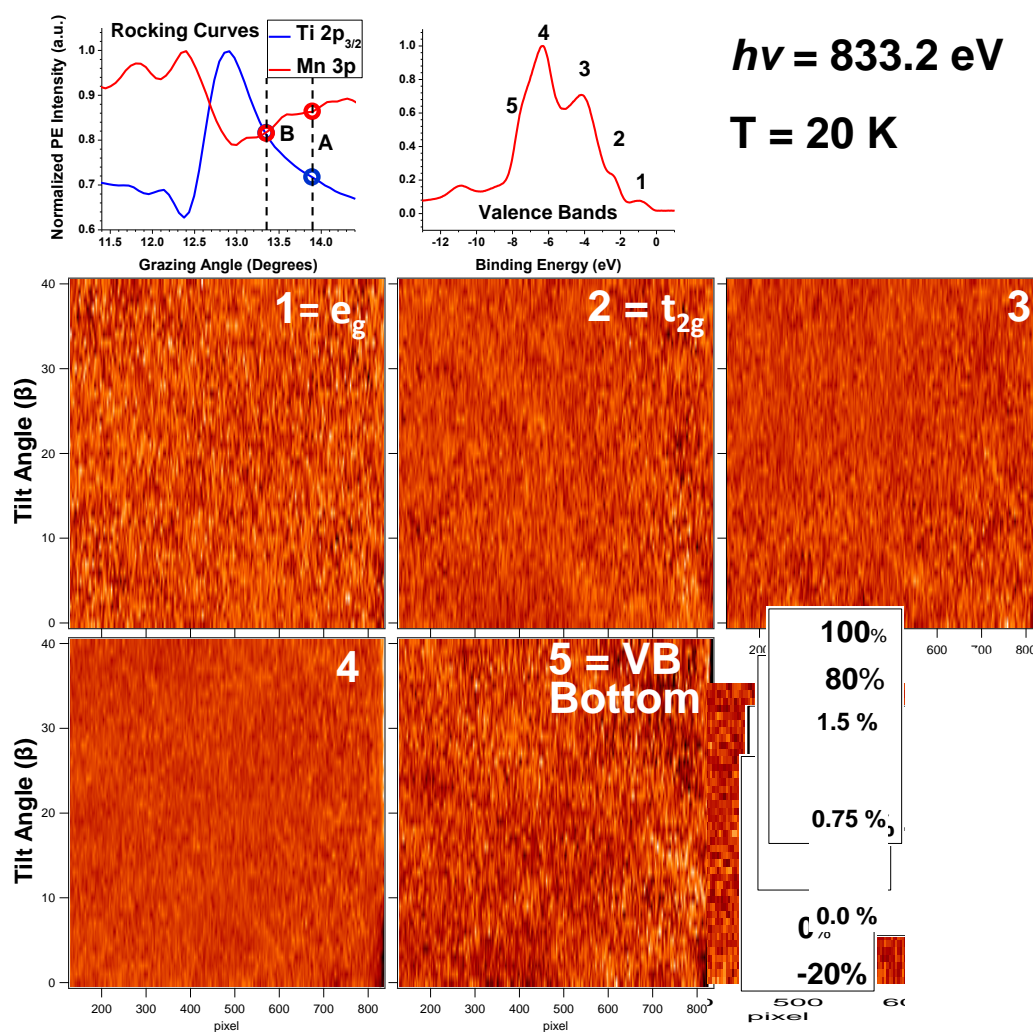**Fig. S4.** As fig. S3, but for the angles C and E exhibiting maximum standing-wave contrast to bulk and interface.

Figure S5

Fig. S5. As fig. S3, but for the angles A and B that should both be more sensitive to the LSMO/STO interface.
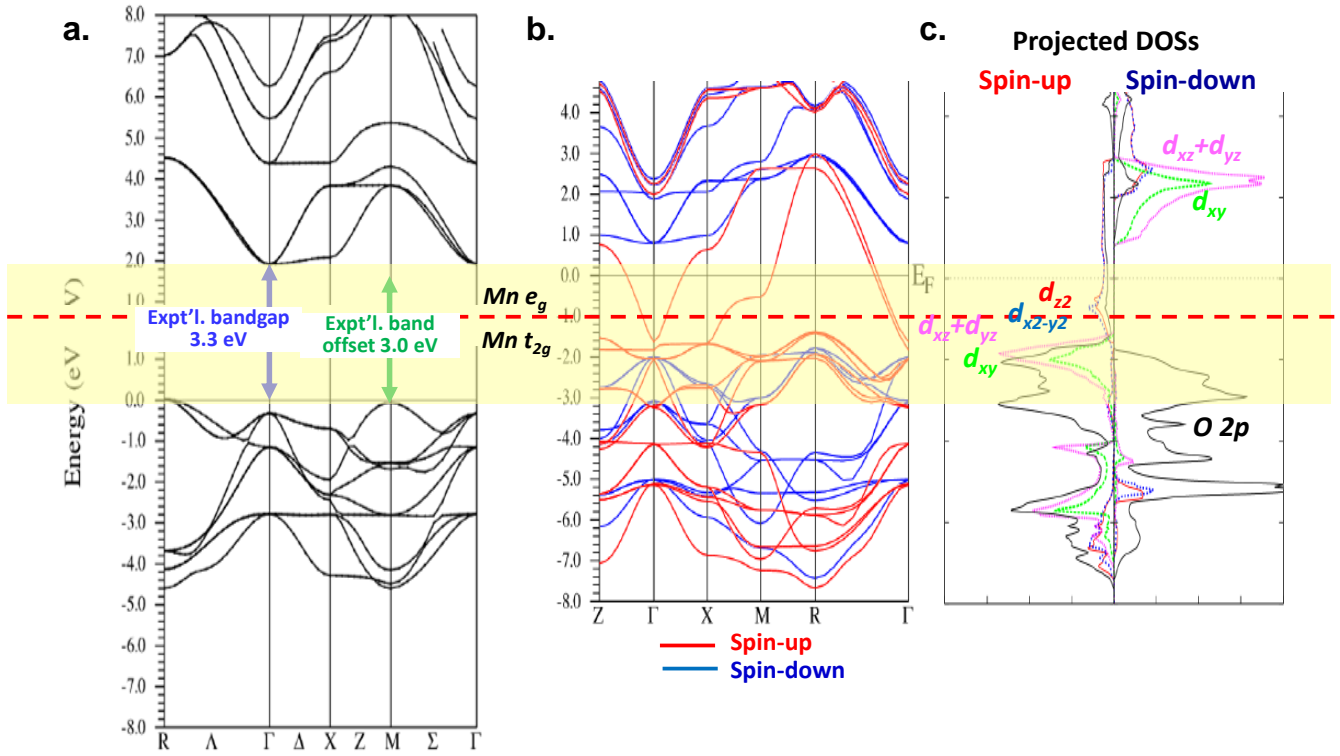
Figure S6

Fig. S6. The LDA band structures of (a) the band-insulator STO and (b) the half-metallic ferromagnet LSMO, as calculated with the Wien2k program. The band gap for STO has been adjusted with a scissors operator to agree with the experimental indirect bandgap. The experimental band offset in our sample has been measured using hard x-ray photoemission from core levels and valence bands [15]. The shaded yellow region is that over which the LSMO bands are expected to be seen in our SWARPES data. The calculations for LSMO were done in the LDA+U approximation. (c) Projected densities of states for LSMO, indicating the expected e_g, t_{2g} and O $2p$ makeup. LSMO is assumed to be ferromagnetic here, even though in our multilayer, it has only weak ferromagnetic order (cf. fig. S9).
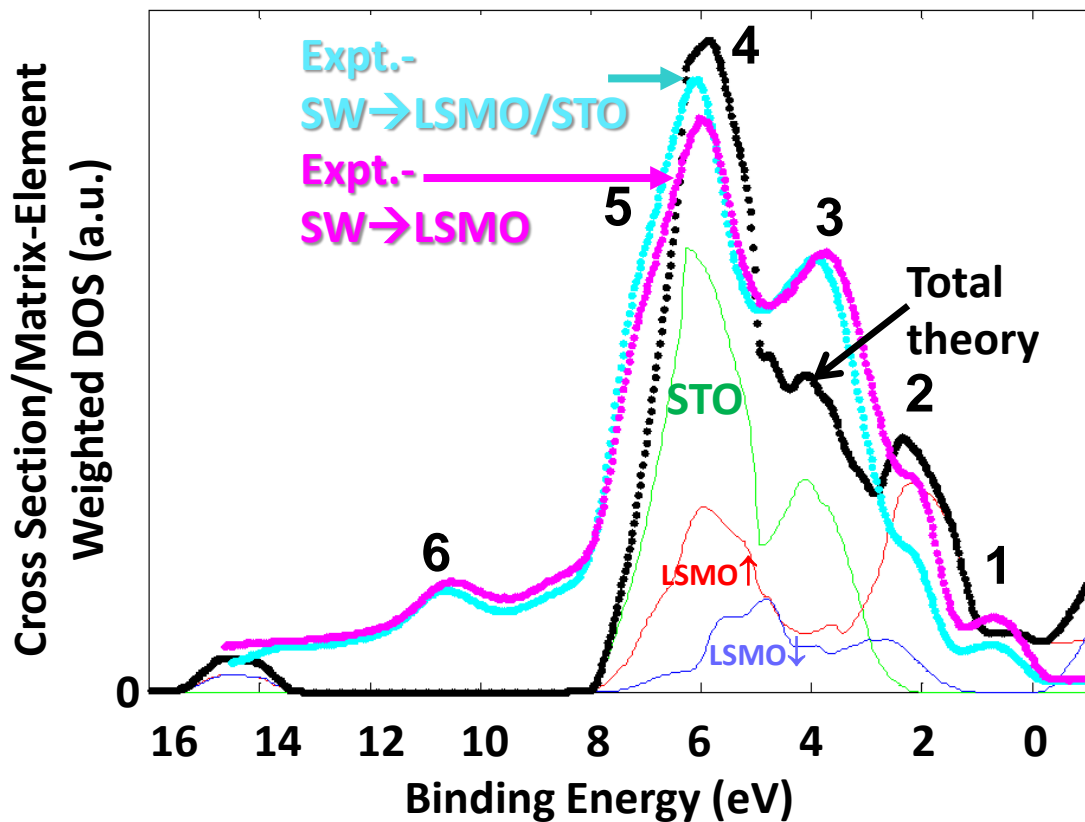
Figure S7

Fig. S7. Comparison of experimental angle-averaged DOS-like spectra at angles C (interface) and E (bulk) with LDA densities of states from the calculations of fig. S6 that have been summed with cross section and inelastic attenuation corrections over the 4 unit cell/4 unit cell structure of our multilayer. These show the dominance of LSMO over ca. 0-3 eV, and of STO for greater binding energies. Theory here is in error by about 4.5 eV for the O-2*s* dominated band 6 at about 10.5 eV in experiment, but this is not relevant to our SWARPES data.
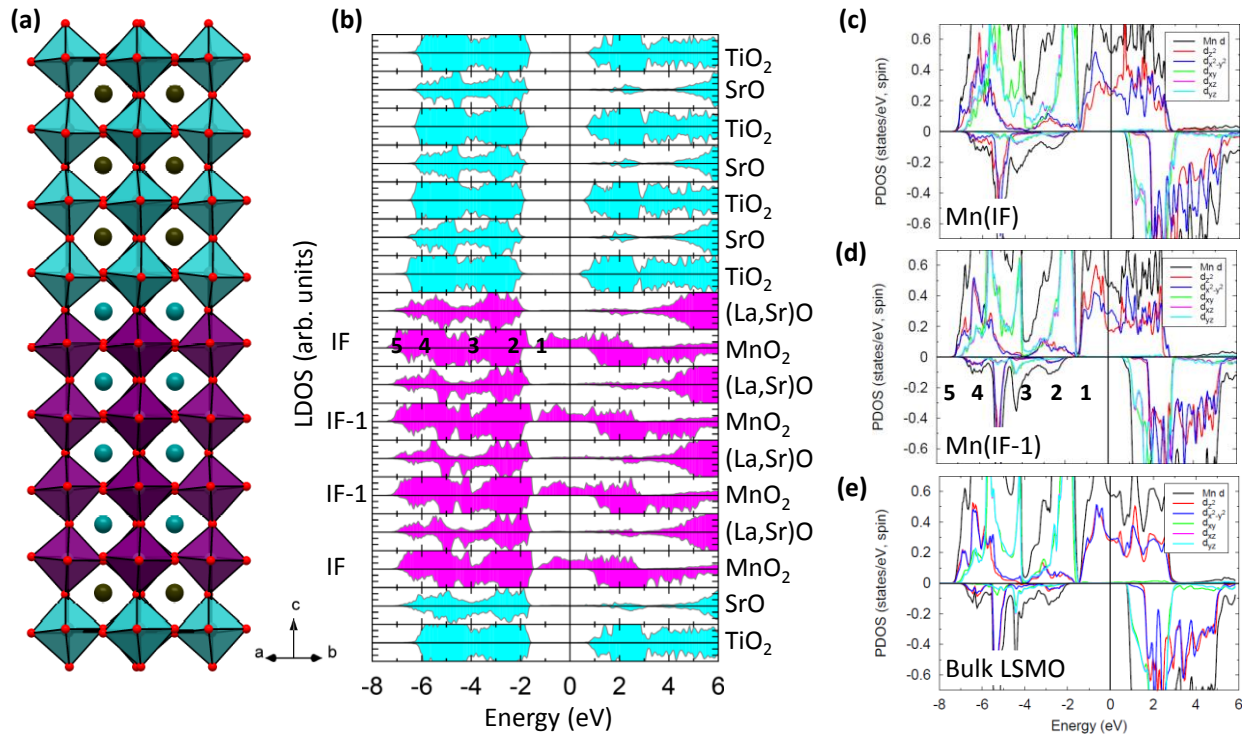
Figure S8

Fig. S8. Results from fully self-consistent all-electron GGA+U calculations for a 4 u.c. LSMO/4 u.c. STO multilayer. (a) Side view of the relaxed structure of the superlattice. (b) The layer-resolved total densities of states (LDOS), with Mn-containing layers at the interface (IF) and center "bulk" layers (IF-1) indicated. (c),(d) Projected densities of states for Mn summed over (c) the two interfaces IF, (d) the two center/bulk layers IF-1, and (e) for bulk LSMO. The energy positions at which we have chosen to show SWARPES results are indicated as 1-5 in (b) and (d). Note that the DOS due to the lowest-lying LSMO bands near the point R (see fig. S6) are expected to be below those of STO.
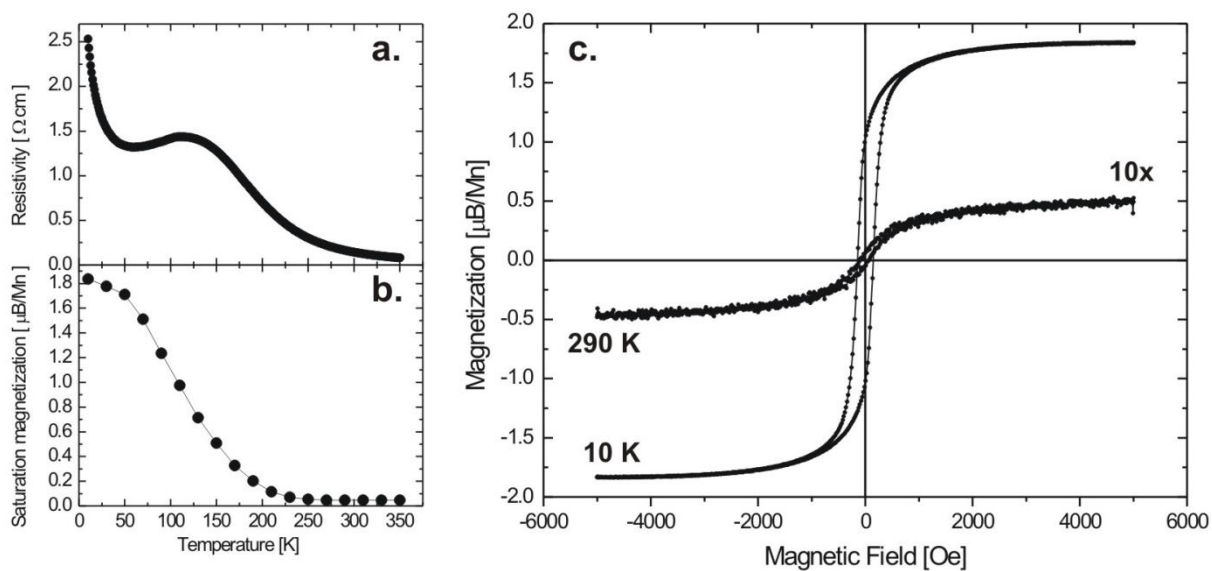
Figure S9

Fig. S9. Electrical transport and magnetic properties of the LSMO/STO superlattice. (a),(b) Temperature dependence of the resistivity and saturation magnetization respectively. (c) Magnetic hysteresis loops at 10 and 290 K showing ferromagnetic behavior.
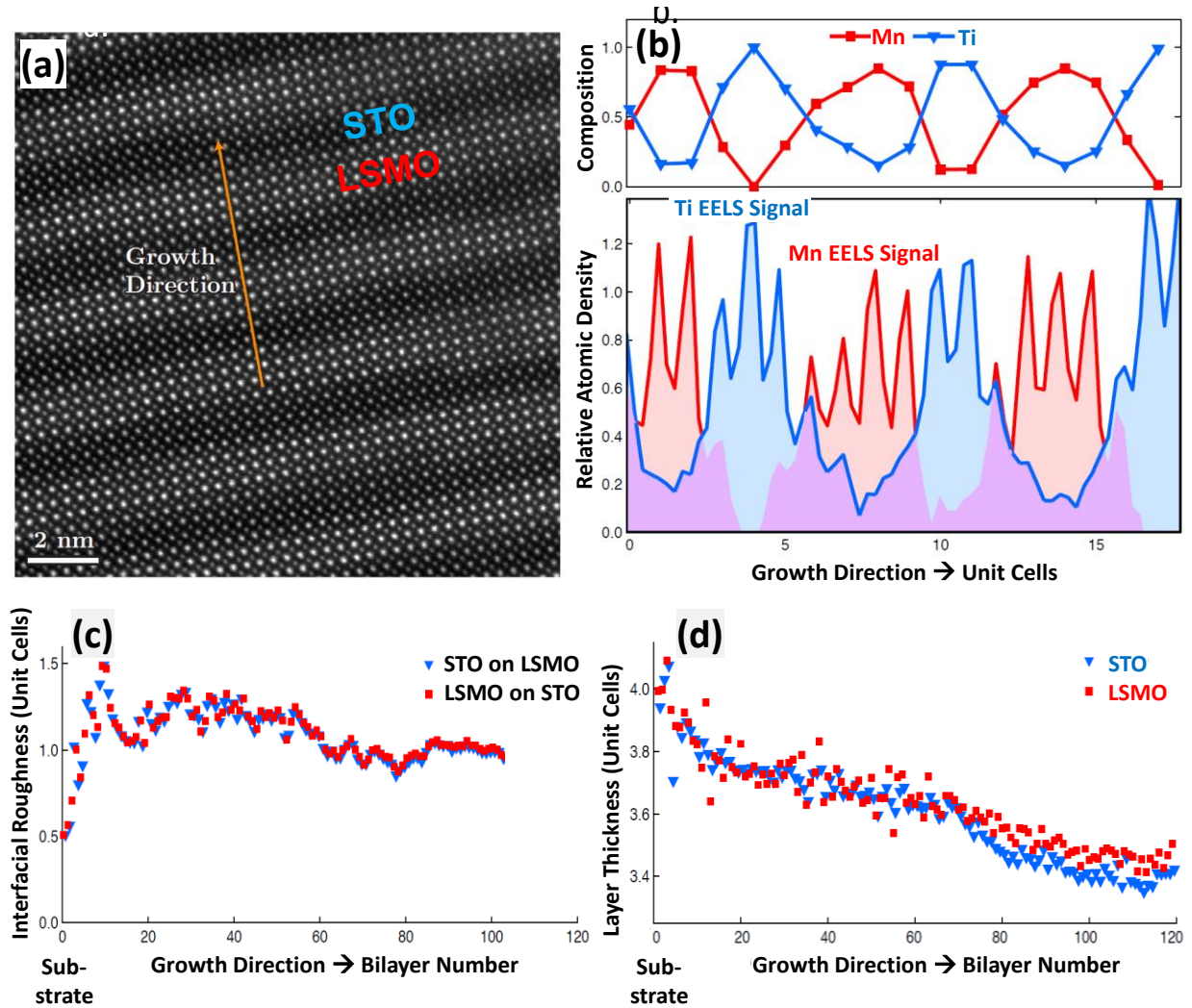
Figure S10

Fig. S10. (a) High resolution HAADF-STEM micrograph of the LSMO/STO sample in cross-section near the 90th grown layer, with the location of the EELS line scan indicated. (b) Ti/Mn column composition calculated from the integration of background-subtracted *L*-edge EELS. (c) Interfacial roughness calculated from the quantitative HAADF-STEM intensities of 800,000 atomic peaks across the full 120 bilayer cross-sectional sample. Roughness is defined as the RMS variance of the intensity midpoint of each bilayer transition, with each layer sampled over at least 200 nm. The steep drop-off after 100 layers is due to a slight bend in the TEM sample from residual stress in the multilayers, and should be ignored. (d) Layer thickness determined from the quantitative HAADF-STEM intensities of 800,000 atomic peaks across the full 120 bilayer cross-sectional sample. Layer thickness is defined as the peak-peak distance between maxima of an envelope function fit to atomic column intensity maxima.